Atomic-Structural Synergy for Catalytic CO Oxidation over Palladium–Nickel Nanoalloys

Shiyao Shan,[†] Valeri Petkov,[‡] Lefu Yang,[†,§] Jin Luo,[†] Pharrah Joseph,[†] Dina Mayzel,[†] Binay Prasai,[‡] Lingyan Wang,[†,#] Mark Engelhard,[||] and Chuan-Jian Zhong*,[†]

[†]Department of Chemistry, State University of New York at Binghamton, Binghamton, New York 13902, United States
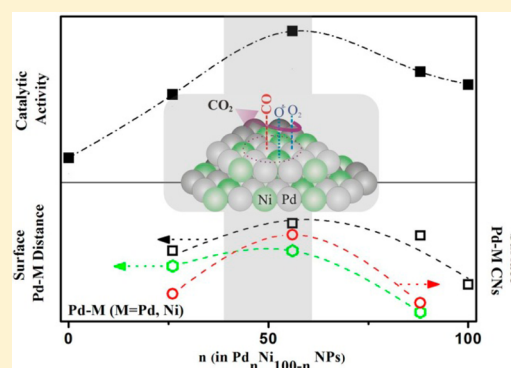[‡]Department of Physics, Central Michigan University, Mt. Pleasant, Michigan 48859, United States
[§]College of Chemistry and Chemical Engineering, Xiamen University, Xiamen 361005, China
[||]EMSL, Pacific Northwest National Laboratory, Richland, Washington 99352, United States

S *Supporting Information*

ABSTRACT: Alloying palladium (Pd) with other transition metals at the nanoscale has become an important pathway for preparation of low-cost, highly active and stable catalysts. However, the lack of understanding of how the alloying phase state, chemical composition and atomic-scale structure of the alloys at the nanoscale influence their catalytic activity impedes the rational design of Pd-nanoalloy catalysts. This work addresses this challenge by a novel approach to investigating the catalytic oxidation of carbon monoxide (CO) over palladium–nickel (PdNi) nanoalloys with well-defined bimetallic composition, which reveals a remarkable maximal catalytic activity at Pd:Ni ratio of ∼50:50. Key to understanding the structural-catalytic synergy is the use of high-energy synchrotron X-ray diffraction coupled to atomic pair distribution function (HE-XRD/PDF) analysis to probe the atomic structure of PdNi nanoalloys under controlled thermochemical treatments and CO reaction conditions. Three-dimensional (3D) models of the atomic structure of the nanoalloy particles were generated by reverse Monte Carlo simulations (RMC) guided by the experimental HE-XRD/PDF data. Structural details of the PdNi nanoalloys were extracted from the respective 3D models and compared with the measured catalytic properties. The comparison revealed a strong correlation between the phase state, chemical composition and atomic-scale structure of PdNi nanoalloys and their catalytic activity for CO oxidation. This correlation is further substantiated by analyzing the first atomic neighbor distances and coordination numbers inside the nanoalloy particles and at their surfaces. These findings have provided new insights into the structural synergy of nanoalloy catalysts by controlling the phase state, composition and atomic structure, complementing findings of traditional density functional theory studies.

1. INTRODUCTION

In comparison with platinum (Pt), palladium (Pd) based catalysts have attracted increasing attention for petrochemical processing, fuel cell reactions, and automotive exhaust treatments. This is reflected by a surge of interest in alloying Pd with different transition metals for preparation of low-cost, highly active and stable catalysts.[1−15] In particular, Pd alloyed with transition metals such as nickel (Ni) and copper (Cu) in various bimetallic compositions has already been explored in heterogeneous catalytic reactions such as oxygen reduction, alcohol oxidation, methane combustion, and hydrogenation reactions,[4−19] paralleling studies of Pt-based alloy catalysts.[20,21] Theoretical studies based on a localized single layer of alloyed Pt and Ni have suggested an increase of oxygen adsorption strength with relative Ni contents,[22] but no clear indication of structural synergy for CO oxidation. One interesting study has shown that the adsorption energy of oxygen and CO on Pd−Ni alloys varies with the bimetallic composition, revealing a

minimum at Pd:Ni ratio close to 1:1 indicating good potential for high activity for CO oxidation reaction.[23] Similar findings have been reported in theoretical studies on Pd−Cu alloys.[24] In a recent density functional theory (DFT) study on CO oxidation over a sandwich-type model of Pd−Ni alloys featuring planes of Pd(111) alloyed with Ni,[23] a compressive strain (∼5%) has been found to be beneficial for CO oxidation reaction, whereas a strain beyond 7% distorts the alloy's surface so significantly that the adsorption sites for the CO oxidation reaction diminish. In another recent DFT study on a model of graphene-supported M-Pd$_{12}$ (where M = Fe, Co, Ni, Cu, Zn, Pd) alloy particle,[25] it has been found that alloying enhances the catalyst's stability and activity for oxygen reduction reaction (ORR). Defects in the graphene support anchoring the M-Pd$_{12}$ particle have also been shown to produce a strong particle-

substrate interaction leading to an increase in the particle's stability, shifting in the d-band center, and weakening the adsorption of oxygen species. Also, the study of the adsorption of O and OH on PtNi surfaces by DFT in terms of surface and subsurface alloying[22] has revealed a strong dependence of the strength of adsorption for both O and OH on the type of the subsurface's atomic planes in the order of Pt(111)-skin-Pt_3Ni < Pt(111) < Pt_3Ni(111) < PtNi(111) < $PtNi_3$(111) < Ni(111). There is a downshift in d-band center at this subsurface alloy due to the formation of a Ni monolayer on the subsurface of Pt(111). How this model operates for Ni on Pd(111) is yet to be studied. Interestingly, in an earlier DFT study of the stress induced nanostructures and the formation energy of epitaxial Pd adlayer on Ni(110) surface,[26] the energy has been found to be at minimum when Pd−Pd first atomic neighbor distance was 2.72 Å. Moreover, study of the effect of Pd−Ni(111) surface segregation on the catalytic activity for CO hydrogenation[19] has demonstrated that as little as 5 at % of Pd incorporated in Ni(111) surface may increase the activity by as much as 4 orders of magnitude. The enhanced activity has been attributed to 3-fold hollow sites with three Pd or two Pd atoms and one Ni atom as nearest neighbors for the HCOs hydrogenation step. These theoretical studies have provided some insights into the structural impact of alloying of Ni into Pd on the surface adsorption. None of the prior studies of Pd−Ni nanoalloys, however, have indicated the presence of a strong correlation between the phase state, chemical composition and atomic-scale structure of PdNi nanoalloys and their catalytic activity.

To gain an insight into the structural synergy in the PdNi nanoalloys, there is a clear need to establish the composition dependence of both the atomic structure and the catalytic activity. In this respect, the findings of a recent DFT study on the catalytic activity of PdCu alloy for ORR[24] drew our attention. The study has showed that Cu reduces Pd−O binding energy, whereas Pd increases Cu−O binding energy due to charge transfer from Pd to Cu. It is the increased overlap between the d-states of Pd and the adsorbed oxygen that makes the reduction of binding energy at Pd sites more significant than the increase of binding energy at Cu sites and, hence, the ORR activity optimal at Pd:Cu ratio of 1:1. In addition, studies of the so-called lattice strain effect on the reactivity of Pd−Cu alloys with Pd-rich surface[27] also drew our attention. The study indicated that the adsorption strengths of OH_{ads} and O_{ads} and the magnitude of strain in Pd−Cu alloys, measured in terms of face-centered-cubic (fcc) lattice constant, are strongly correlated. Moreover, considering the fact that the reaction rate of catalytic oxidation of CO over Pd follows $[O_2][CO]^{-1}$ in terms of kinetics,[28] the surface reaction of adsorbed CO and O_2 species determines the activation energy, though there is an inhibition effect of CO adsorption on the rate at low reaction temperatures. The competitive adsorption of excessive CO blocks the activation of oxygen, especially at low temperature. In order to enable the catalyst surface with optimal active sites for both reactant species, a fundamental question is how the catalytic activity is influenced by the bimetallic composition and the atomic-scale structure at the nanoalloy surface. It is therefore imperative to reveal how Pd and Ni atoms are arranged not only inside but also at the surface of the PdNi nanoalloy particles and how this arrangement operates synergistically when the catalyst is probed, for example, with CO oxidation reaction.[29,30] In the present study, knowledge of the atomic arrangement in nanoalloy particles was obtained by high-energy X-ray diffraction coupled to atomic pair distribu-

tion function (HE-XRD/PDF) analysis and reverse Monte Carlo (RMC) simulations, as demonstrated powerfully for a number of other nanoalloy particles.[31−34] Particular attention was paid to understanding how exactly Pd and Ni atoms cooperate synergistically for effective activation and maneuvering of surface CO and O species through structural and chemical composition effects.

2. EXPERIMENTAL SECTION

Chemicals. Palladium(II) acetylacetonate ($Pd(acac)_2$, 97%), octyl ether ($[CH_3(CH_2)_7]_2O$, 99%), oleylamine ($CH_3(CH_2)_7CH\ CH(CH_2)_8NH_2$, 70%), 1,2-hexadecanediol (90%), and oleic acid ($CH_3(CH_2)_7CH\ CH(CH_2)_7COOH$, 99+%) were purchased from Aldrich. Nickel(II) acetylacetonate ($Ni(acac)_2$, >95%) were purchased from Alfa Aesar. Other chemicals such as ethanol, hexane, and potassium choloride were purchased from Fisher Scientific. Vulcan carbon XC-72 was obtained from Cabot. Pd (20% on activated carbon (Pearlman's catalyst), unreduced, 50% water wet paste (Escat 1951, BASF Kit)) was obtained from Strem Chemicals. Gases of CO (1 vol % balanced by N_2) and O_2 (20 vol % balanced by N_2) were obtained from Airgas. All chemicals were used as received.

Synthesis of PdNi Nanoparticles and Preparation of Catalysts. The synthesis of Pd_nNi_{100-n} nanoparticles followed a protocol reported previously.[35] Briefly, palladium(II) acetylacetonate and nickel(II) acetylacetonate were mixed in a desired molar ratio into octyl ether solution. The composition of the Pd_xNi_{100-x} nanoparticles was controlled by the feeding molar ratio. Oleic acid and oleylamine were added as capping agents and 1,2-hexadecanediol as a reducing agent under N_2 atmosphere. The solution was purged with N_2 and heated first to 100 °C. The mixture was then heated to 220 °C and refluxed for 30 min. After the solution cooled back to room temperature, the resulting Pd−Ni NPs were precipitated out by adding ethanol followed by centrifugation. The NPs were redispersed in hexane solvent for further use.

To prepare carbon supported NPs, controlled amount of PdNi nanoparticles was mixed with carbon (XC-72) in a hexane solution followed by sonication and overnight stirring. The resulting carbon supported PdNi NPs, hereafter referred as PdNi/C NPs, were collected and dried under N_2 atmosphere. The activation of Pd_nNi_{100-n}/C NPs was achieved by thermochemical processing described elsewhere.[36] Typically, PdNi/C NPs were first treated at 120 °C under N_2 to remove the organic solvent, then kept at 260 °C under 20 vol % O_2 for 1 h to remove the organic capping molecules on the NP surface, and finally calcined at 400 °C under 15 vol % H_2 for 2 h. Commercial Pd/C, which was treated at 400 °C under 15 vol % H_2 for 1 h, was used for comparison. The average size of commercial Pd/C NPs used was about 7 nm. The weight loadings of most PdNi/C catalysts studied in this work were within 20−37%. (e.g., 37% for $Pd_{26}Ni_{74}$/C and $Pd_{56}Ni_{44}$/C, 33% for $Pd_{88}Ni_{12}$/C, 20% for Pd/C, and 4% for Ni/C). The exact mass loading was determined by thermogravimetric analysis (TGA) performed on a PerkinElmer Pyris 1-TGA.

Catalytic Activity Measurement. The catalytic activity of the Pd_nNi_{100-n}/C catalysts was measured under CO (0.5 vol % balanced by N_2) + O_2 (10 vol % balanced by N_2) using a customer-built system including a temperature-controlled reactor, a gas flow/mixing/injection controller, and an online gas chromatograph (Shimadzu GC 8A) equipped with 5A molecular sieve and Porapak Q packed columns and a thermal conductivity detector. The catalysts were loaded in a quartz microreactor tubing (inner diameter: 4 mm) and wrapped with quartz wool at both ends in the center of the tubing (length of the catalyst bed: ∼6 mm). The feeding gas (0.5 vol % CO + 10 vol % O_2 balanced by N_2) was injected continuously through the fixed catalyst's bed in the quartz microreactor at a flow rate of 20 mL/min. The residence time was about 0.2 s. Gas hourly space velocity (GHSV) in the system was around 16 000 h^{-1}. The CO conversion was determined by analyzing the composition of the tail gas effusing from the quartz microreactor packed with the catalyst's fixed bed by the online gas chromatograph.

Morphology and Composition Characterization. High-angle annular dark-field scanning TEM (HAADF-STEM) was employed to determine the morphology of the Pd_nNi_{100-n}/C NPs and catalysts. Maps of elemental distribution in Pd−Ni NPs were obtained by energy dispersive X-ray spectroscopy (EDS). The samples were prepared by dropping cast of ethyl alcohol suspension of carbon supported nanoparticles onto a carbon-coated copper grid followed by solvent evaporation at room temperature. The measurements were performed on FEI Titan G2 80−200 Chemi-STEM electron microscope at 200 kV.

Inductively Coupled Plasma−Optical Emission Spectroscopy (ICP-OES). ICP-OES was used to analyze the chemical composition of the Pd−Ni NPs. The analysis was performed on a PerkinElmer 2000 DV ICP-OES instrument using a cross-flow nebulizer with the following parameters: plasma 18.0 L $Ar_{(g)}$/min; auxiliary 0.3 L $Ar_{(g)}$/min; nebulizer 0.73 L $Ar_{(g)}$/min; power 1500 W; peristaltic pump rate 1.40 mL/min. Laboratory check standards were analyzed for every 6 or 12 samples, with instrument recalibration if the standards were not within ±5% of the initial concentration.

X-ray Photoelectron Spectroscopy. XPS measurements were performed ex situ using a Physical Electronics Quantum 2000 scanning ESCA microprobe. This system uses a focused monochromatic Al Kα X-ray (1486.7 eV) source for excitation and a spherical section analyzer. The instrument has a 16-element multichannel detection system. The X-ray beam used was a 100 W, 100-μm in diameter beam. It was rastered over a 1.4 mm by 0.2 mm rectangle spot on the sample. The X-ray beam was incident normal to the sample, and the X-ray detector was at 45° away from the normal. The binding energy (BE) scale was calibrated using C 1s peak at 284.8 eV as internal standard. The percentages of individual elements detected were determined by analyzing the areas of the respective XPS peaks.

In Situ and Ex Situ Structure Characterization Using Synchrotron High-Energy XRD (HE-XRD). HE-XRD measurements were carried out in both ex situ ($\lambda = 0.1115$ Å) and in situ ($\lambda = 0.1378$ Å) modes at the beamlines 11-ID-C and 11-ID-B, respectively, at the Advanced Photon Source, Argonne National Laboratory. For the ex situ experiments PdNi/C samples were loaded into thin, one end open glass capillaries. A reactor-type cell described by Oxford et al.[37] was used in the in situ experiments. In this case PdNi/C samples were loaded into a 7 cm long quartz tube with a diameter of 1 mm allowing free flow of gases through the NP samples. Ceramics-based heaters on both sides of the tubes were used to heat the sample to a particular temperature. Gas type, gas flow rate, heating rate and temperature were carefully monitored and controlled during measurements.

The collected XRD patterns were reduced to the so-called structure factors, $S(q)$, and then Fourier transformed to atomic PDFs $G(r)$, using the relationship:

$$G(r) = \frac{2}{\pi} \int_{q=0}^{q_{max}} q[S(q) - 1] \sin(qr)\, dq \tag{1}$$

,where $q_{max}= 25$ Å^{-1} is the maximum wave vector reached in the present experiments. Note atomic PDFs $G(r)$ are experimental quantities that oscillate around zero and show positive peaks at real space distances, r, where the local atomic density $\rho(r)$ exceeds the average one ρ_o. This behavior can be expressed by the equation $G(r) = 4\pi r\rho_o[\rho(r)/\rho_o - 1]$, which is the formal definition of the PDF $G(r)$. Here $\rho(r)$ and ρ_o are the local and average atomic number density, respectively. High-energy XRD and atomic PDFs have already proven to be very efficient in studying the atomic-scale structure of nanosized materials, including metallic alloy NPs.[38,39]

3. RESULTS AND DISCUSSION

3.1. Morphology and Composition. The bulk composition of the Pd_nNi_{100-n} nanoparticles was first determined by ICP-OES. Figure 1 shows a representative plot of n in Pd_nNi_{100-n} NPs as determined by ICP-OES vs the norminal feeding in terms of the atomic fraction m (i.e., mPd and $(100 - m)$Ni) in the NP synthesis. The data show an approximate 1-
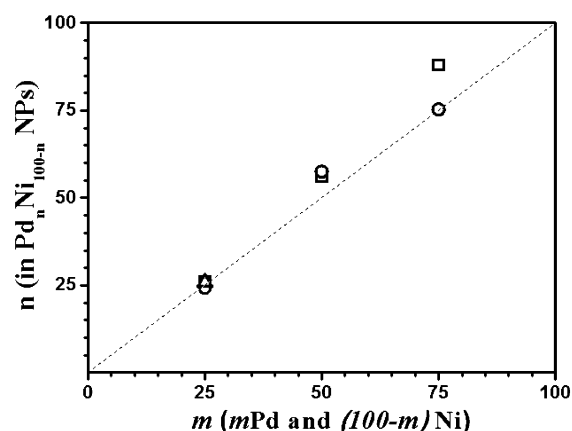

Figure 1. Plot of n in Pd_nNi_{100-n} nanoparticles as determined by ICP-OES vs the norminal feeding in terms of the atomic fraction m (i.e., mPd and $(100 - m)$Ni) in the NP synthesis. The dahsed line represents a 1:1 relationship.

to-1 relationship, demonstrating that the chemical composition of the binary alloy PdNi NPs can be controlled well by controlling the feeding ratio of the metal precursors in the synthesis. For the purposes of this work we concentrated on Pd_nNi_{100-n} NPs with $n = 26, 56$ and 88.

The average sizes of the supported nanoparticles were determined by analyzing data from different HAADF-STEM images, showing 7.1 ± 1.1, 5.9 ± 1.0, 5.4 ± 1.3 nm for $Pd_{26}Ni_{74}$, $Pd_{56}Ni_{44}$, and $Pd_{88}Ni_{12}$, respectively. The subtle increase of the particle sizes, as compared with those of the as-synthesized particles, was due to thermal sintering of the nanoparticles during the thermochemical treatments. A representative set of HAADF-STEM image for $Pd_{26}Ni_{74}$/C, $Pd_{56}Ni_{44}$/C and $Pd_{88}Ni_{12}$/C NPs is shown in Figure 2 and Figure S1 (Supporting Information, SI). As evidenced by the elemental mapping data, the nanoparticles are largely random PdNi nanoalloys. There is no apparent indication of surface enrichment.

The above assessement was further substantiated by XPS analysis of the relative surface composition of Pd_nNi_{100-n}/C nanoparticles ($n = 26, 56$ and 88) (Figure S2 (SI)). As shown in Table 1, the relative ratio of Pd and Ni species in Pd_nNi_{100-n} NPs determined by XPS, which is mostly sensitive to the surface, is rather close to that determined by ICP-OES analysis, which is representative of the chemical composition of bulk NPs. This finding confirms the largely random alloy character of Pd_nNi_{100-n} nanoparticles ($n = 26, 56$ and 88).

Second, both the Pd 3d peak and Ni 2p position are found to shift slightly to a higher binding energy with increasing Ni %. For Ni, however, the presence of not only Ni(0) but also of Ni(+2) surface species can be inferred from the XPS data. The latter suggests a certain degree of partial oxidation of surface Ni atoms, which is likely due to air exposure of the samples before XPS measurements.

3.2. Catalytic Oxidation of CO. CO oxidation was used as a probe reaction to understand how the different atomic ratio of Pd and Ni in Pd_nNi_{100-n} NPs ($n = 26,56$ and 88) influences their catalytic activity. Catalytic activity was measured on PdNi/C catalysts treated at 260 °C under O_2 atmosphere only and further treated at 400 °C under H_2 atmosphere. Figure 3 shows a representative set of CO conversion data for a $Pd_{25}Ni_{75}$/C catalyst, starting from a fresh state, i.e., the NPs supported on carbon but not thermochemically treated.
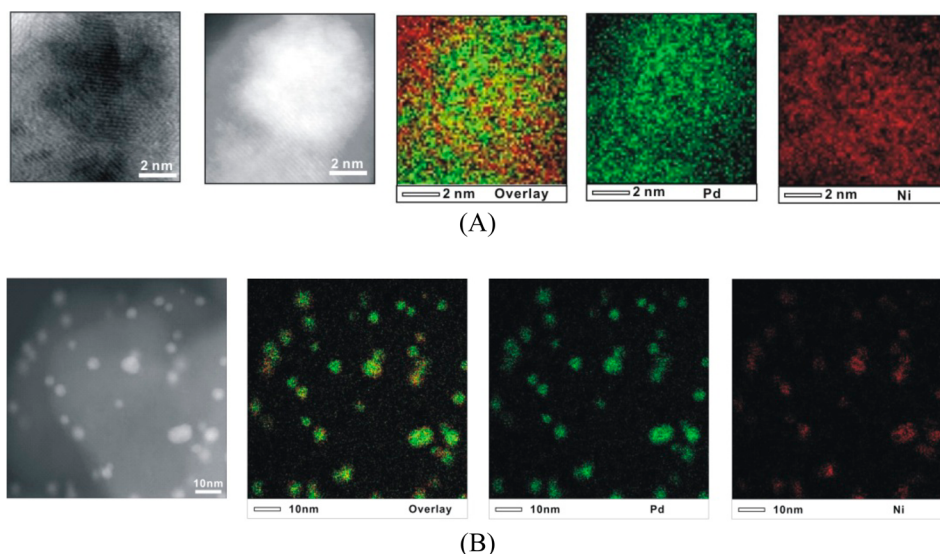
(A)

(B)

Figure 2. High-angle annular dark field scanning HAADF-STEM images (left) and elemental maps (right) for carbon-supported $Pd_{26}Ni_{74}$ (A) and $Pd_{56}Ni_{44}$ (B) nanoparticles (Ni species in red and Pd species in green).

Table 1. XPS Peak Positions (Binding Energy in eV) and Relative Atomic Ratios of Pd:Ni in the Pd_nNi_{100-n}/C Nanoparticles

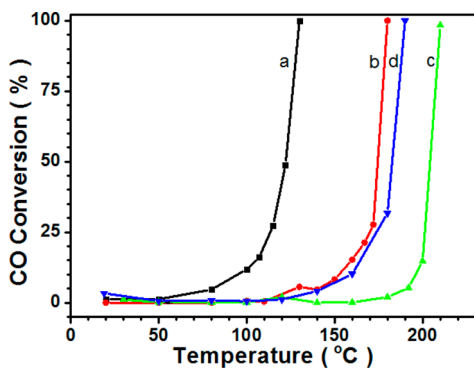| catalyst	Pd 3d ($3d_{3/2}$, $3d_{5/2}$)	Ni $2p_{3/2}$	atomic ratio Pd:Ni
$Pd_{26}Ni_{74}$	341.2, 335.9	856.6	24:76
$Pd_{56}Ni_{44}$	341.1, 335.9	856.4	49:51
$Pd_{88}Ni_{12}$	341.0, 335.8	856.4	86:14

Figure 3. CO conversion for a fresh $Pd_{25}Ni_{75}$/C thermally treated under several different conditions: (a) under O_2 at 260 °C for 30 min, (b) further treated at 400 °C for 30 min under H_2, (c) under O_2 at 450 °C for 30 min only, and (d) further treated at 300 °C for 30 min under H_2.

The catalytic activity for $Pd_{25}Ni_{75}$/C treated at 260 °C under O_2 atmosphere only is significantly higher than that for the same catalyst subjected to further treatment at 400 °C under H_2 atmosphere. This is well demonstrated by the clear difference in the "half-conversion" temperature (T_{50}), at which 50% of CO conversion is achieved. The fresh sample was not catalytic active because the NPs surfaces were covered by capping molecules. After the initial O_2 treatment, the light-off temperature (i.e., T_{10}, the temperature at which 10% conversion is achieved) was below 100 °C, and the half-conversion (50%) was achieved at 120 °C (Figure 3, curve a). The subsequent treatment under H_2 at 400 °C was found to cause a distinct deactivation, as shown by an increase of 54 °C

in T_{50} (Figure 3, curve b). A further oxidation treatment led to a further deactivation (Figure 3, curve c, $T_{50} \sim 204$ °C). However, this oxidation-induced deactivation could be recovered (Figure 3, curve d, $T_{50} \sim 180$ °C) by H_2 reduction at 300 °C. The results suggest that there were possibly two types of oxygenated surface sites for the oxidized PdNi NPs in comparison with the reduced ones. One type had a higher activity for CO oxidation but was irreversibly destroyed at a higher temperature, and the other had a lower activity but could be reversibly converted to the site upon reduction in the thermochemical treatment.

On the other hand, changing the parameters and/or sequence of the thermochemical treatment was shown to tune the catalytic activity significantly, as evidenced by the observations of $T_{50} \sim 204$ °C for $Pd_{25}Ni_{75}$/C catalyst treated under O_2 and ~ 180 °C for that treated under H_2 atmosphere. Note treatment under O_2 atmosphere did not lead to "burning" of the carbon support, as evidenced by TGA data shown in Figure S3 (SI). The tunability of the catalytic activity is further examined by comparing the data for CO conversion over monometallic and bimetallic NP catalysts, including Ni, Pd and Pd_nNi_{100-n}/C (n = 26, 56 and 88) treated under O_2 or H_2 atmosphere (Figure 4). The data show that the catalytic activity for CO oxidation depends on both the catalyst composition and the oxidation/reduction state. Since nickel is not a good catalyst for oxidation reaction due to a large barrier to redox cycle, the catalytic activity for CO oxidation is prominently undertaken by palladium. Interestingly, when palladium is alloyed with nickel, a remarkable enhancement of the activity is observed (Figure 4A). With the increase of Ni in PdNi nanoalloy, the catalytic activity for CO oxidation is increased. $Pd_{56}Ni_{44}$/C shows a light-off temperature below 80 °C, which is lower than single palladium catalyst by nearly 60 °C. However, a negative effect is observed when excessive Ni is introduced into PdNi alloy, as evidenced by an increase of the light-off temperature to 140 °C for $Pd_{26}Ni_{74}$/C catalyst, which is 60 °C higher than that of $Pd_{56}Ni_{44}$/C, and even much higher than those of both commercial Pd/C and Pd/C prepared similarly (Figure S4 (SI)). An optimal Ni-composition in the PdNi alloy would lead to a balance of CO and O_2 adsorption potentials. The increase of Ni could increase the coverage of oxygen as a
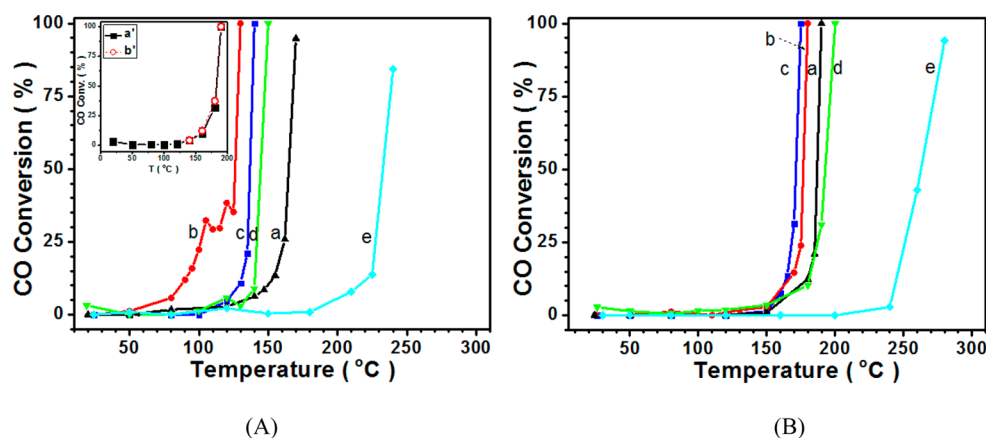
Figure 4. CO conversion over $Pd_{26}Ni_{74}/C$ (black, a), $Pd_{56}Ni_{44}/C$ (red, b), $Pd_{88}Ni_{12}/C$ (blue, c), Pd/C (green, d), and Ni/C ((cyan, e) catalysts treated under H_2 (A) and O_2 (B). Inset in A: CO conversion activities for $Pd_{25}Ni_{75}/C$ treated under H_2, comparing data collected by increasing (black solid line, a′) and descreasing (red dash line, b′) the reaction temperatutre.
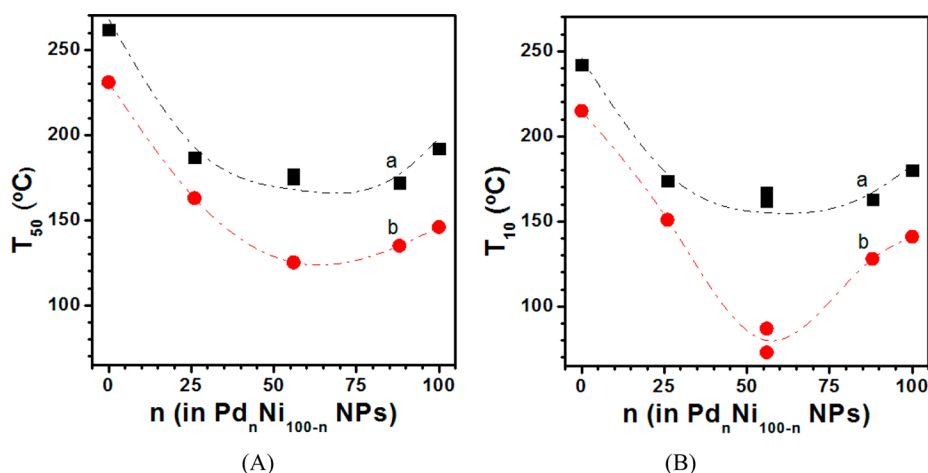

Figure 5. Plots of T_{50} (A) and T_{10} (B) vs n for Pd_nNi_{100-n}/C catalysts treated under O_2 at 450 °C for 30 min (a, black), and under H_2 at 300 °C for 30 min (b, red).

result of increased oxophilicity, promoting reaction with CO adsorbed on Pd. However, if Ni exceeds a threshold, the CO adsorption becomes critical limiting total reaction. This is reflected by the data in Figure 4B for the oxygenated PdNi NPs after the oxidation treatment, leading prominently to a drop of the catalytic activity. In fact, due to the resistance to reduction of oxygenated active phase, an osillation of the activity was observed below T_{50} for CO oxidation over H_2 treated $Pd_{56}Ni_{44}/$ C. Clearly, the consideration of both T_{10} and T_{50} is useful for better assessing the catalytic activities. This finding indicates that the activity is quite sensitive to the balance of the surface redox competition of metals and the evolution of active phase on PdNi nanoalloy.

The data in Figure 4 for PdNi/C catalysts also show that the temperature range for CO conversion is unusually narrow. This is evidenced by the rapid rise of CO conversion rate in the temperature range from the light-off temperature to the temperature for 100% conversion, which is ~10 °C. To the best of our knowledge such a narrow temperature range for CO conversion has not been observed for alloy catalysts. For comparison, the temperature range for CO conversion over pure Pt and Pt-based alloy catalysts is usually 40−60 °C.[20,21] Such narrow range may be due to a rise of temperature ("hot spot") in the catalyst column that activates the catalyst under a

high gas flow rate by desorption of poisoneous species off the surface of the catalyst. However, the flow rate (0.5 vol % CO +10 vol % O_2 at GHSV = 16 000 h^{-1}) in our work was relatively slow in comparison with earlier studies on CO and NO oxidation over $PdCu/CeO_2−ZrO_2$ and $PdNi/CeO_2−ZrO_2$ catalysts that used 1% CO + 0.45% O_2 + 0.1% NO at a flow rate of 30 000 h^{-1}, showing a temperature range of ~60 °C.[40] In addition, we tested the reversibity of CO conversion activity for $Pd_{25}Ni_{75}/C$ NPs by collecting data both during temperature increase and descrease. The respective data sets overlap with each other (see Figure 4A inset), demonstrating a complete reversibility. This observation suggests that the surface adsorption was under a equilibrium condition. A further transient study is needed to gain a deeper insight into the surface adsorption with respect to the observed narrow temperature range for CO conversion over the PdNi/C nanoalloy catalysts.

The catalytic activities of CO oxidation over Pd_nNi_{100-n}/C NPs were assessed further by comparing values of T_{50} or T_{10} at which 50% or 10% of CO conversion is achieved, respectively. Figure 5 shows a typical set of data for T_{50} and T_{10} vs Pd % on Pd_nNi_{100-n}/C nanoalloy catalysts. The catalysts were prepared by treatment at 260 °C under O_2 followed by H_2 at 400 °C and then exposed to air before being

Table 2. Comparison of Kinetic Parameters for CO Oxidation over Pd/C and PdNi/C Catalysts

catalysts	d_{NPs}[a] (nm)	thermal treatment	avg D (dispersion, %)[a]	reaction rate (10^{-5} mol g_{Pd}^{-1} s^{-1})[b] ($T_{\sim 100\%}$, °C)	TOF ($\times 10^{-2}$ s^{-1})[c] ($T_{\sim 100\%}$, °C)	E_a (kJ mol^{-1})
Pd	~7.0	H_2	16	2.27 (150)	1.52 (150)	28.1 (41.4[d])
$Pd_{26}Ni_{74}$	7.1 ± 1.1	O_2–H_2	16	3.01 (170)	2.04 (170)	21.4 (32.5[d])
$Pd_{56}Ni_{44}$	5.9 ± 1.0	O_2–H_2	19	1.76 (130)	0.99 (130)	8.7 (5.2[e]) (5.88[d])
$Pd_{88}Ni_{12}$	5.4 ± 1.3	O_2–H_2	21	1.48 (140)	0.76 (140)	19.8 (44.7[d])

[a]The dispersion of Pd on the surface of one NP was calculated using $D = (6V_m/(a_m d)) \times 100\%$, where V_m is the volume of atom Pd, a_m is Pd surface area, and d is the particle size [b]Calculation of reaction rate was based on moles of CO reacted at the flow rate and was normalized against the total mass of Pd in the catalyst. [c]Calculation of TOF was based on the surface Pd using TOF = reaction rate/(MW(Pd) × D). Note that the metal loading (20−37%) is significantly higher than usual (0.1−8%), leading to a higher percentage of buried nanoparticle surface in this work. [d]Data derived from plots of exponential fitting of the rate vs temperature. [e]Data derived from low temperature range in plots of ln R vs 1/T for $Pd_{56}Ni_{44}$ NPs.
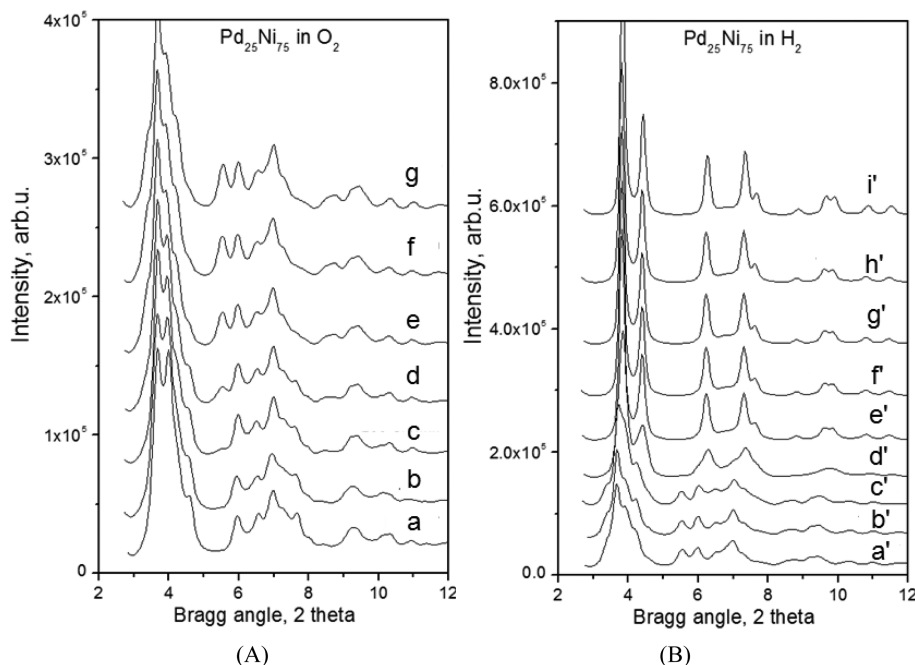

Figure 6. In situ HE-XRD patterns obtained during thermochemical treatment of fresh $Pd_{25}Ni_{75}$/C NPs first under O_2 (A) and then under H_2 (B) atmosphere. The thermochemical treatment sequence is as follows: (A) (a) room temperature, (b) 100 °C, (c) 1 min at 260 °C, (d) 10 min at 260 °C, (e) 20 min at 260 °C, (f) 30 min at 260 °C, and (g) back to room temperature; (B) (a′) room temperature, (b′) 100 °C, (c′) 200 °C, (d′) 300 °C, (e′) 400 °C, (f′) 10 min at 400 °C, (g′) 20 min at 400 °C, (h′) 30 min at 400 °C, and (i′) back to room temperature.

loaded into the catalyst test bed, and were further treated under H_2 or O_2 before the CO conversion measurements. It is evident that T_{50} or T_{10} for the Pd−Ni/C NPs treated under H_2 exhibits a minimum near 50% Pd, which corresponds to a maximum in terms of the catalytic activity. A similar trend is observed with PdNi/C catalysts treated under O_2. In this case, the composition at which the minimum in T_{50} or T_{10} seemed to shift to a higher Pd%. Nevertheless, the observation of minimum in T_{50} or T_{10}, or maximum in catalytic activity, indicates a catalytic synergy of the PdNi nanoalloy.

Kinetic data were obtained for CO oxidation by analyzing the reaction rate as a function of reciprocal temperature (also see Figure S5 (SI)). Generally, a linear dependence between ln(R) and 1/T was observed ("R" is Pd-specific mass rate for CO oxidation), especially at higher reaction temperatures. At lower reaction temperatures a slight deviation from linearity was observed. In contrast to previous studies of binary and ternary Pt-alloy catalysts,[41] the subtle deviation from linearity is not completely clear, but is thought to be associated with the narrow temperature range observed for CO oxidation over these catalysts. Table 2 summarizes the results for the activation energy (E_a) and TOFs (Turnover frequency).

Note that the data (e.g., reaction rate and TOF) in Table 2 were extracted from somewhat different temperature regions because of the narrow temperature range of CO oxidation and the differences in T_{50} among the different catalysts (see Figure 4). As such, the data in Table 2 may not be directly compared one vs another. In general, the activation energy for Pd/C appears somewhat smaller than those reported for Pd/Al$_2$O$_3$ catalyst[41] and different from those of single-crystal Pd.[42] Again, among the catalysts, $Pd_{56}Ni_{44}$/C shows the lowest activation energy, which explains the highest catalytic activity exhibited by this catalyst. Note that activation energy is independent of the temperature within a certain range. The activity maximum coincides with the 50:50 ratio in terms of activation energy (see Figure 4 and Table 2).

3.3. Phase State and Atomic Structure of Pd_nNi_{100-n}/C NPs Revealed by Ex and In Situ HE-XRD/PDFs Experiments Coupled to Computer Simulations. To understand the intriguing catalytic synergy of Pd and Ni species in Pd_nNi_{100-n}/C NPs for CO oxidation, the NP atomic-scale structure was studied by ex and in situ HE-XRD coupled to atomic PDFs analysis and computer simulations.
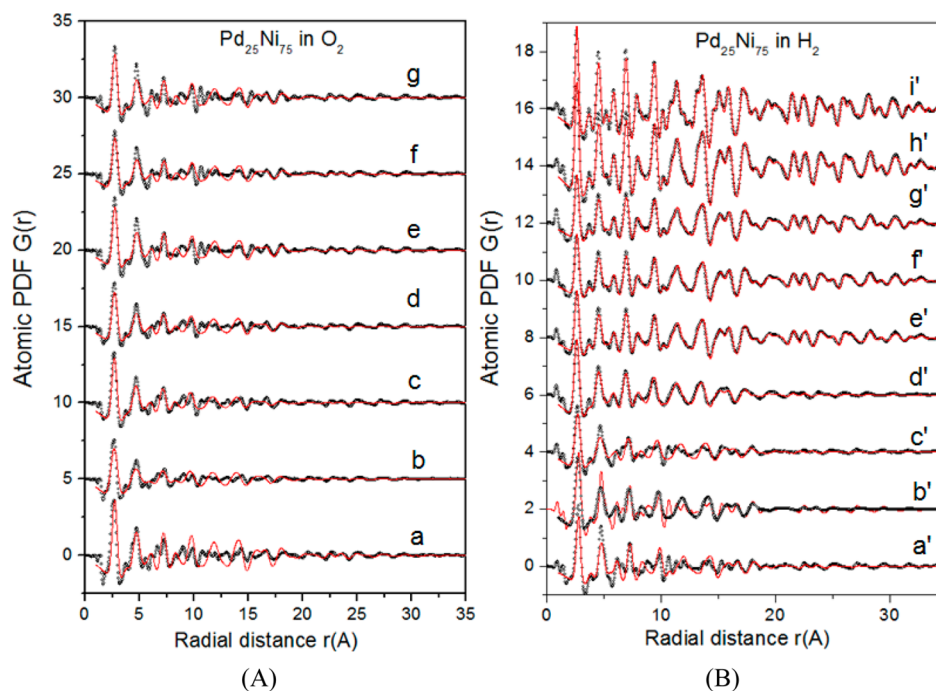
Figure 7. Experimental atomic PDFs (black dots) and fcc-type model computed atomic PDFs (lines in red) for fresh $Pd_{25}Ni_{75}/C$ catalyst: (A) first treated under O_2 up to 260 °C, and (B) further treated under H_2 up to 400 °C. The thermochemical treatment sequence is as follows: (A) (a) room temperature, (b) 100 °C, (c) 1 min at 260 °C, (d) 10 min at 260 °C, (e) 20 min at 260 °C, (f) 30 min at 260 °C, and (g) back to room temperature (O_2); (B) (a′) room temperature, (b′) 100 °C, (c′) 200 °C, (d′) 300 °C, (e′) 400 °C, (f′) 10 min at 400 °C, (g′) 20 min at 400 °C, (h′) 30 min at 400 °C, and (i′) back to room temperature.

(A). In Situ HE-XRD/PDFs Studies on the Evolution of Atomic Structure Type and Phase State. The evolution of the phase state in terms of the alloying structure and the atomic-structure of the PdNi/C NPs starting from nonthermally treated state, i.e., before being thermally treated, to thermally treated states under different thermochemical treatment conditions, e.g., treatment at 260 °C under O_2 followed by treatment at 400 °C under H_2, was studied by in situ HE-XRD/PDFs. Figure 6 shows a representative set of HE-XRD patterns obtained during thermal treatment of $Pd_{25}Ni_{75}/C$ NPs first in O_2 (A) and then in H_2 atmosphere (B). The fresh $Pd_{25}Ni_{75}/C$ NPs exhibits a multiphase character. The phase segregation is evidenced by the "triplet" Bragg peak at about 4° (2θ), and the cluster of peaks in the region of 6−8° (2θ), where θ is the Bragg diffraction angle. Upon heating to 260 °C under O_2, HE-XRD patterns evolve considerably, reflecting an evolution of the atomic structure in $Pd_{25}Ni_{75}/C$, but the multiphase character of NPs remains unchanged (see Figure 6A). Upon further heating to 400 °C under H_2, the NPs gradually turn into a single phase, face centered cubic (fcc)-type PdNi nanoalloy (see Figure 6B). The atomic arrangement in the single-phase $Pd_{25}Ni_{75}/C$ NPs becomes more closely packed; i.e., the interatomic distances "shrink" somewhat, when heating at 400 °C is prolonged for about 30 min. The interatomic distance "shrinking" is largely preserved when the fcc-type nanoalloy particles are cooled back to room temperature.

To obtain a clearer insight into the structural evolution of fresh $Pd_{25}Ni_{75}$ NPs under the thermal processing conditions described above, the experimental HE-XRD patterns were reduced to the so-called atomic PDFs, shown in Figure 7. Furthermore, the experimental atomic PDFs were approached with a structure model based on fcc-type atomic structure. On the basis of the PDFs data analysis (Figure 7A), and the

numerical results from the fits to the experimental PDFs, the structural "evolution" of the catalysts under heating in O_2 involved the following stages. First, the as-synthesized sample at room temperature is phase segregated, and the PDF data cannot be fit well with a fcc-type model alone. Nevertheless, the fcc-type model would yield an estimated "lattice parameter" of $a = 3.870$ Å in this particular case. The first PDF peak, which reflects the first atomic coordination sphere, is very broad and "positioned" at 2.65 Å. Second, heating to 100 °C in O_2 atmosphere does not change $Pd_{25}Ni_{75}/C$ NPs much structurally. Here, the fcc-type model yields an estimated "lattice parameter" of $a = 3.873$ Å. The very broad first PDF peak is positioned at 2.66 Å. Third, upon treating at 260 °C prolonged from 1 to 30 min, NPs become less phase segregated. Here the estimated "lattice parameter" evolves from 3.876 to 3.865, then to 3.888, and finally to 3.898 Å for heating time of 1, 10, 20, and 30 min, respectively. The first PDF peak becomes narrower and its position evolves from 2.69 to 2.72, then to 2.76, and finally to 2.77 Å, respectively, indicating a significant structural evolution toward a more uniform state from a structural point of view. Finally, upon being cooled back to room temperature, $Pd_{25}Ni_{75}/C$ NPs keep the level of phase segregation attained at 260 °C. Accordingly, the respective atomic PDF data is not well approximated with fcc-type model alone. The estimated "fcc-lattice parameter" is 3.888 Å and the first PDF peak is positioned at 2.76 Å. Details of these changes are included in Table S1 (SI). In summary, thermal treatment of fresh $Pd_{25}Ni_{75}/C$ NPs in O_2 does not result in dramatic but gradual change in the NP phase state and atomic-scale structure.

The fresh $Pd_{25}Ni_{75}/C$ NPs, after being thermally treated under O_2, were further treated under H_2 up to 400 °C. Switching O_2 to H_2 atmosphere at room temperature does not change the phase-segregated character of NPs as shown by the

data in Figures 6B and 7B. Upon heating to 300 °C, experimental XRD data indicate a very significant phase/structural change, as evidenced by the sudden turn of the "triplet" Bragg peak at about 4° 2θ into a "doublet" and the disappearance of the "cluster "of peaks in the region of 5−8° 2θ (Figure 6B). This change reflects the turning of the initially phase-segregated $Pd_{25}Ni_{75}/C$ NPs into single phase nanoalloys. The degree of crystallinity improves upon further heating to 400 °C. NPs remain single phase nanoalloys when cooled down back to room temperature. Analysis of the respective atomic PDFs and the numerical results of the fcc-type model fits allow a more precise identification of the structural "evolution" of the NPs treated under H_2 atmosphere. (1) At room temperature and after treatment up to 100 °C, NPs keep the level of phase segregation attained during the treatment in O_2 atmosphere, and hence, atomic PDF data may not be well fit with a fcc-type model. Here, the still quite broad first PDF peak is positioned at about 2.77 Å. (2) Increasing the temperature to 200 °C nearly turns the NPs into a single phase, fcc-type nanoalloy. The quality of fcc-model based fits to the experimental data improves significantly, and the "fcc-lattice parameter" shrinks from 3.877 Å at 100 °C to 3.821 Å at 200 °C. The position of first PDF peak evolves from 2.73 Å at 100 °C to 2.71 Å at 200 °C. (3) Upon heating to 300 °C, phase segregation disappears completely, and the NPs turn into a fcc-type nanoalloy that, however, appears somewhat disordered locally. Experimental PDF data can be fully accounted for by a fcc-type model with a fcc lattice parameter $a = 3.712$ Å. First PDF peak narrows and becomes more symmetric in shape, indicating that the first atomic coordination sphere in the NPs straightens out. Its radius, as estimated from the position of first PDF peak, is 2.61 Å, indicating a sudden "shrinking" of the interatomic distances (in comparison with the 200 °C treated NPs where the first PDF peak is positioned at 2.71 Å). The sudden "shrinking" suggests a sharp, i.e., first-order like, transition of "two-phase" NPs to a "single" phase, fcc-type nanoalloy NPs. (4) Further treating the NPs at 400 °C for 10 to 30 min improves their crystallinity only. The respective atomic PDF data are almost perfectly fit with a fcc-type model. Fcc-lattice parameters extracted from the fits hardly change (i.e., from 3.724 to 3.724 and then to 3.724 Å for heating time of 10, 20, and 30 min, respectively). At the same time the first PDF peak becomes more and more narrow and symmetric in shape, indicating further straightening out of the first atomic coordination shell in the NPs. The position of that peak remains largely unchanged (i.e., from 2.62 to 2.62 and then to 2.61 Å for heating time of 10, 20, and 30 min, respectively). (5) Upon cooling back to room temperature, the NPs remain single phase, fcc-type nanoalloys of very good crystallinity. Atomic PDF data are perfectly fit with a fcc-type model, yielding fcc-lattice parameter of 3.702 Å. The width of the first PDF peak is significantly reduced due to the lower level of atomic thermal vibrations at room temperature as compared to 400 °C.

Distinct first atomic neighbor distances of about 2.5 and 2.7 Å are clearly seen as two components of the fairly broad and asymmetric first peak of the experimental atomic PDFs for the fresh $Pd_{25}Ni_{75}/C$ NPs after being thermally treated under O_2 (see Figure 7A and Table S1 (SI)), as it may be expected for PdNi NPs consisting of segregated Ni-rich and Pd-rich phases. Thermal treatment under O_2 decreases the asymmetry of first PDF peak, and that under H_2 completely removes it, resulting in the two distinct first atomic neighbor distances "merging" into a single one of ∼2.61 Å, which is very close to the

arithmetic mean of Pd−Pd (2.75 Å) and Ni−Ni (2.48 Å) distances in bulk Pd and Ni. The latter suggests that the fcc-type atomic structure of thermally treated, single-phase $Pd_{25}Ni_{75}/C$ NPs is most likely to be of a random alloy character.

The in situ HE-XRD data provided a structural basis for comprehending the differences in the catalytic activity for the PdNi/C catalysts treated under O_2 and H_2 atmospheres. It is the change of the phase state of PdNi NPs from segregated to single phase, fcc-type nanoalloy that is responsible for the observed differences in the catalytic activity. In particular, PdNi NPs treated under O_2 are phase segregated, presumably into Ni-rich and Pd-rich phases, with one of the phases being more active catalytically than the other. As it will be discussed later, Pd-rich phase with first atomic neighbor distance of about 2.7 Å is likely to be more active catalytically than Ni-rich phase with first atomic neighbor distance of about 2.5 Å. Thermal treatment in H_2 turns the phase-segregated PdNi NPs into single-phase NPs of fcc-type, random alloy structure where the first atomic neighbor distance is about 2.6 Å, eventually leading to a reduced catalytic activity (see Figures 3 and 4).

To understand the phase state/atomic-scale structure effect on the catalytic synergy, we examined the viability of a refined thermal treatment protocol for improving the catalytic activity. In this experiment the fresh $Pd_{25}Ni_{75}/C$ NPs were activated catalytically by thermal treatment first under N_2 (inert atmosphere) at 260 °C and then under H_2 atmosphere at 400 °C, i.e., no initial oxidative treatment before the reduction. As shown in Figure 8, the catalytic activities of the $Pd_{25}Ni_{75}/C$
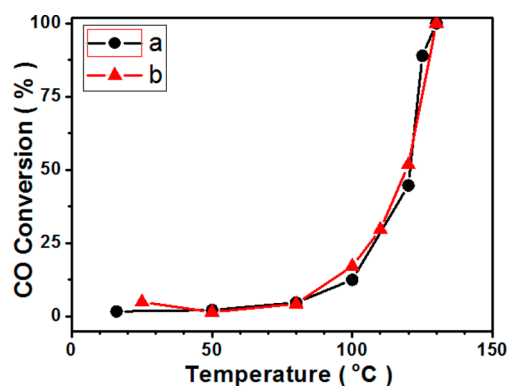

Figure 8. CO conversion data for a $Pd_{25}Ni_{75}/C$ NPs activated by thermal treatment under N_2 at 260 °C for 1 h and then in H_2 at 400 °C for 2 h and then (1) thermally treated first in O_2 at 260 °C for 1 h (black, a); and (2) further treated in H_2 at 400 °C for 2 h (red, b) (flow rate of CO and O_2 mixture: 14 mL/min).

catalyst after being treated under O_2 (Figure 8, *curve a*) and further under H_2 (Figure 8, *curve b*) are comparable, which are in fact remarkably similar to that of $Pd_{25}Ni_{75}/C$ catalyst treated under O_2 only (see Figure 3).

In this case, the phase state and atomic-scale structure type of the catalyst are largely retained at a catalytically very active state (i.e., a "phase-segregated/inhomogeneous atomic structure" state) due to the absence of the initial oxidation. The good reproducibility of catalytic activity under repetitive cycles of the redox treatment is indicative of a high resistance to oxidative-induced deactivation. In this case, HE-XRD/PDF analysis provides both local and extended structure information across the entire nanoparticles. In comparison, XAFS is a more local structure sensitive spectroscopic technique that provides
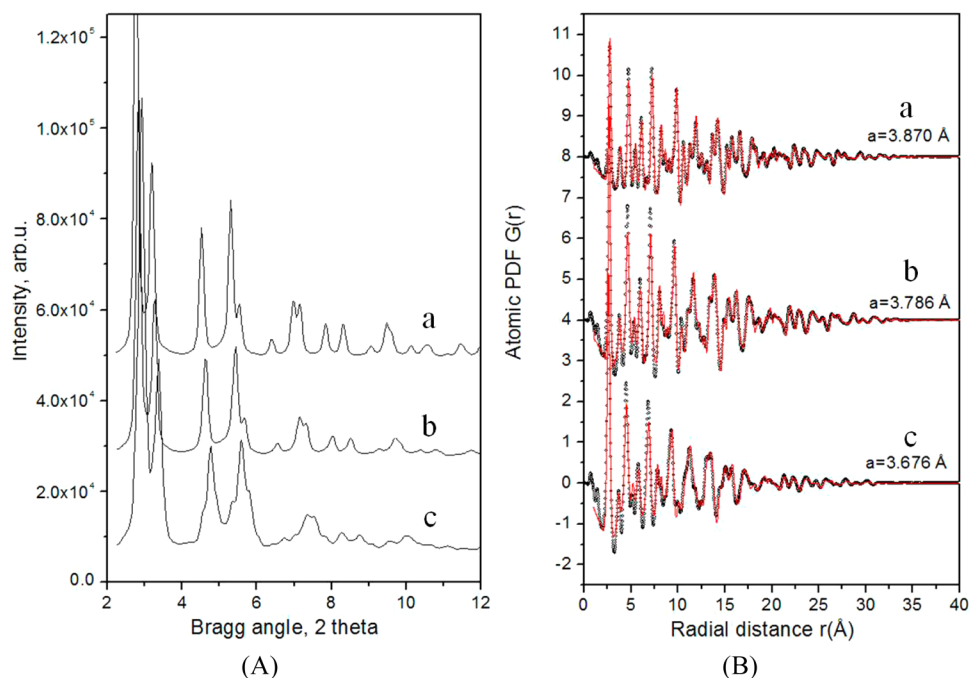
Figure 9. (A) Experimental HE-XRD patterns and (B) Experimental (black dots) atomic PDFs and fcc-lattice based (solid line in red) atomic PDFs for catalytically activated, single phase $Pd_{88}Ni_{12}$ (a), $Pd_{56}Ni_{44}$ (b) and $Pd_{26}Ni_{74}$ (c) NPs.
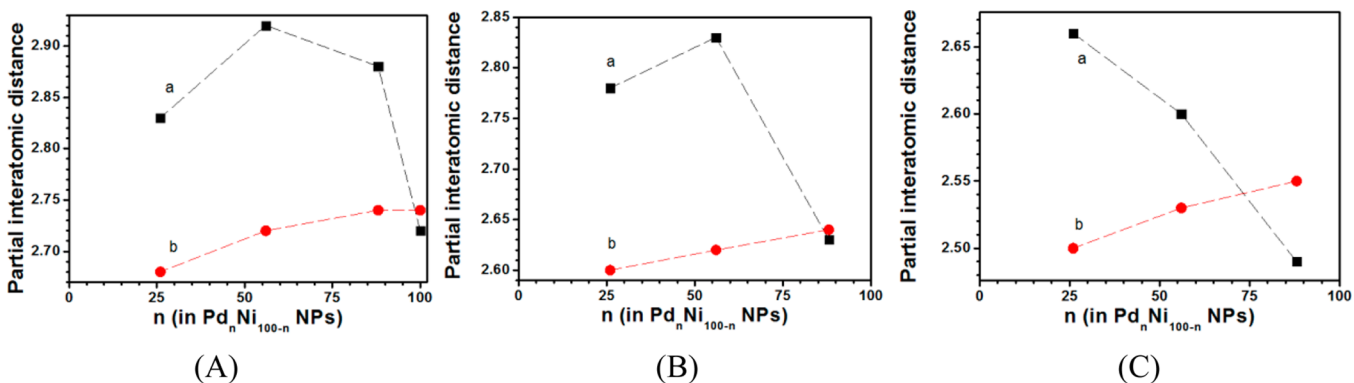

Figure 10. First M−M atomic neighbor distances extracted from RMC constructed structure models for $Pd_n Ni_{100-n}$NPs, including Pd−Pd (A), Pd−Ni (B), and Ni−Ni(C) distances between atoms at the NP surface (black, a) and across the entire NP (red, b), as a function of the bimetallic composition (n).
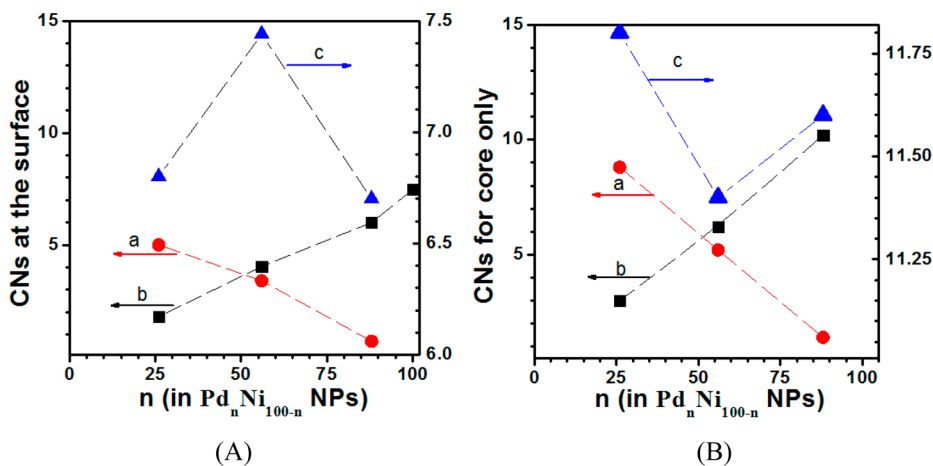

Figure 11. Partial Pd−Ni (red, a) and Pd−Pd (black, b) CNs and average total Pd CNs (blue, c), obtained by their addition, for Pd atoms at the surface (A), and in the core (B) of Pd_nNi_{100-n} NPs. CNs are obtained from the RMC simulated, 3D structure models of PdNi NPs.

chemical state and local structure information for selected elements. In our recent reports,[20,43−47] XAFS was used to study the oxide formation and local coordination number of several Pt-based binary (e.g., PtNi) and ternary (e.g., PtNiCo) nanoalloy catalysts from which useful information on the alloying properties could be derived, which were quite consistent with the HE-XRD/PDF analysis results. A further study of the phase and chemical structures of the PdNi nanoalloys by XAFS is part of our ongoing work.

(B). Structural Features of NP Core and Surface as Revealed by RMC Simulations. Having established the phase state and type of the atomic structure of PdNi NP catalysts, including their evolution under controlled thermochemical treatment conditions, we concentrated on analyzing the atomic structure inside and at the surface of PdNi NPs in terms of partial interatomic distances and coordination numbers. Figure 9A shows experimental HE-XRD patterns for $Pd_nNi_{100−n}$ catalysts of three different bimetallic compositions. The respective experimental atomic PDFs are shown in Figure 9B. By approaching the atomic PDFs with a fcc-type structure model, fcc-lattice parameters 3.676, 3.786, and 3.870 Å were obtained for $Pd_{26}Ni_{74}$, $Pd_{56}Ni_{44}$, and $Pd_{88}Ni_{12}$, respectively. The lattice parameters scale nicely with the bimetallic composition by increasing in magnitude with the relative amount of larger Pd atoms. The position of the first peak in the PDFs, $Pd_{26}Ni_{74}$ (2.59 Å), $Pd_{56}Ni_{44}$ (2.67 Å), and $Pd_{88}Ni_{12}$ (2.73 Å), follows the same trend.

To understand how the first atomic neighbor distances and coordination numbers for particular M−M (M = Pd, Ni) atomic species evolve with the bimetallic composition, we modeled the NP atomic structure by reverse Monte Carlo (RMC) simulations using the experimental PDFs as a guide. Details of the RMC simulations will be presented elsewhere. The interparticle distances and coordination numbers for atoms inside NPs and at their surfaces, as obtained from the simulated 3D structure models, are shown in Figures 10 and 11. Clearly, there is a sharp contrast between the evolution of M−M distances inside NPs and at their surface with the bimetallic composition. In particular, first neighbor Pd−Pd and Pd−Ni distances at the NP surface show a maximum at ~50% Pd. On the other hand, the same distances inside NPs increase monotonically with Pd % (see Figure 10).

Partial and average total first coordination numbers for atoms inside PdNi NPs and at their surface alone, as obtained from the respective 3D structure models, are summarized in Figure 11 and Figure S6 (SI). As it may be expected, Pd−Pd CNs increase and Pd−Ni CNs decrease with increasing Pd %, while Ni−Ni CNs decrease and Ni−Pd CNs increase with Pd % both for atoms inside and at the NP surface. By averaging over all Pd atoms, total CN of Pd atoms at the NP surface, i.e., CNs including first atomic neighbors of any chemical type, can be obtained. These are 6.8 (i.e., 1.8 (Pd−Pd) + 5.0 (Pd−Ni)) for $Pd_{26}Ni_{74}$ NPs, 7.4 (i.e., 4.0 (Pd−Pd) + 3.4(Pd−Ni)) for $Pd_{56}Ni_{44}$ NPs, and 6.7 (i.e., 6.0 (Pd−Pd) + 0.7 (Pd−Ni)) for $Pd_{88}Ni_{12}$ NPs. As can be seen in Figure 11A, the average total CN of surface Pd atoms exhibits a maximum at Pd/Ni ratio of ~50:50. Therefore, not only the first atomic neighbor distances involving surface Pd atoms appear to be extra elongated, but also the packing of immediate neighbors of surface Pd appears to be densest at Pd/Ni ratio of ~50:50. On the other hand, the average total CN of Pd atoms in the NP core (see Figure 11B) shows a clear minimum at Pd/Ni ratio of ~50:50. Also, the first atomic neighbor distances involving the entire NPs do not

appear to be extra elongated at Pd/Ni ratio of ~50:50. Evidently the atomic ordering about Pd atoms at the surface is not an exact replica of that about Pd atoms in the core of PdNi NPs. This is to be expected since, contrary to the NP core atoms, NP surface atoms have incomplete coordination spheres and, more often than not, are subjected to significant surface relaxation effects. By contrast, neither the average total CN for Ni atoms inside and at the surface of PdNi NPs nor the first atomic neighbor distances involving these atoms exhibit nonlinearity with respect to Pd/Ni ratio (see Figure S6A,B (SI)). The different evolution of the first coordination spheres of Pd and Ni atoms with the bimetallic composition suggests that the interaction of Pd and Ni atoms with their immediate neighbors is different. Note that a change in size may result in a change in coordination number and thus a change in the phase properties. The PDF analysis allows one to assess these structures for the entire nanoparticles before and after the size change, which is also supported by results from RMC simulations.

Distributions of the average (i.e., averaged over all atoms) total (i.e., including atomic species of any type) CNs for surface atoms in the $Pd_nNi_{100−n}$ NPs, which can be used as a "measure" of the roughness of the NP surface, are also analyzed (see Figure S7 (SI)). The relative number of 4- and 5-fold coordinated surface atoms, i.e., the relative number of very sharp corners and steps, are found to display a minimum for Pd:Ni ratio of ~50:50. This finding suggests that the surface atoms of PdNi NPs with Pd:Ni ratio of ~50:50 are likely in a "terrace-like" environment in comparison with the surface atoms of those PdNi NPs with lower and higher Pd:Ni ratios, which are likely in a "step/corner-like" environment.

As shown in Figure 12 for the partial interatomic distances and total first CNs involving Pd atoms at the surface of PdNi NPs in comparison with the data for catalytic CO oxidation, a strong correlation is revealed between the atomic-scale structure and the catalytic activity. The maximum of the interatomic separation and coordination of surface Pd atoms in
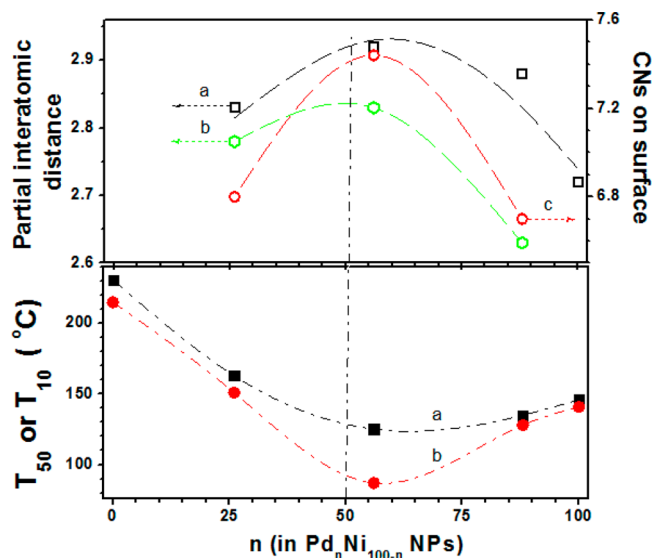

Figure 12. Comparison of partial Pd−Pd (black, a) and Pd−Ni (green, b) interatomic distances and the average total CNs (red, c) for Pd atoms at the surface of $Pd_nNi_{100−n}$ NPs (top panel) with their T_{50} (black, a) and T_{10} (red, b) values for CO oxidation reaction (bottom panel).

Table 3. Summary of Phase State, Chemical and Structural Characteristics of PdNi NPs as Compared to Their Catalytic Activity for CO Oxidation Reaction
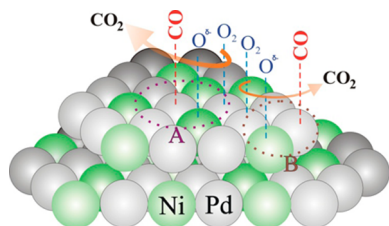
PdNi/support	M−M (Pd−Pd) interatomic distance (surf, Å)	M−M (Pd−Ni) interatomic distance (surf, Å)	Total CNs (surf)	T_{50} (°C)	T_{10} (°C)
PS^a, $Pd_{26}Ni_{74}$				120^b	94^b
SP^a, $Pd_{26}Ni_{74}$	2.83	2.78	6.8	163^c	151^c
SP^a, $Pd_{56}Ni_{44}$	2.92	2.83	7.44	127^c	87^c
SP^a, $Pd_{88}Ni_{12}$	2.88	2.63	6.7	135^c	128^c

^{a}PS: phase segregated, SP: single phase. ^{b}Obtained after treatment under O_2 at 260 °C for 30 min. ^{c}Obtained after treatment under H_2 at 300 °C for 30 min.

PdNi NPs and the minimum of T_{50} and T_{10} values coincide at a Pd/Ni ratio of ~50:50. Apparently, the surface sites with Pd atoms being stretched-out in first coordination sphere radius and having higher coordination numbers, i.e., $Pd_{50}Ni_{50}$ NPs, are more active catalytically than those where the first coordination sphere radius and coordination number of surface Pd atoms are more compact.

3.4. Structural Synergy in Terms of Phase State, Bimetallic Composition, and Atomic Structure for Catalytic CO Oxidation. Taken together, the phase state, bimetallic composition, and atomic-scale structure are shown to be cooperative components responsible for the structural synergy for CO oxidation over the PdNi NP catalysts. As summarized in Table 3, this structural synergy is reflected by cooperativity among three atomic-scale features. First, PdNi NPs segregated into Ni-rich and Pd-rich nanophases exhibit higher catalytic activity than single-phase PdNi NPs of random alloy type structure. Second, the catalytic activity of single-phase PdNi NPs is maximized at a particular bimetallic composition at which the surface Pd atoms are increasingly separated from their immediate neighbors and have increased total first CNs. Finally, single-phase PdNi NPs with a smaller degree of surface structural disorder are more catalytically active than those exhibiting a larger degree of surface structural disorder, i.e., a larger number of unusually low (i.e., 4- and 5-fold) coordinated surface atoms.

As depicted in Scheme 1, the structural synergy for CO adsorption and oxidation over PdNi NPs with Pd/Ni ratio of

Scheme 1^a

^{a}Illustration of the structural synergy for CO adsorption and oxidation over PdNi NPs with Pd/Ni ratio of ~50:50 in terms of high ("A", in a "terrace-like" environment) and low ("B", in a "step/corner-like" environment) coordinated surface atomic sites (Pd atoms in gray, Ni atoms in green). The larger arrow size illustrates the higher catalytic activity for site "A" than for site "B".

~50:50 then can be rationalized in terms of two types of active surface sites: sites with higher CNs labeled as "A" and sites with lower CNs labeled as "B".

Site "A" may be considered more catalytically active than site "B" for two reasons. First, the first neighbor distances involving site "A" atoms, e.g., Pd−Pd and Pd−Ni distances, are elongated

to a greater extent. Increased interatomic distances are usually associated with a d-band upshift and an increase in oxygen binding energy, as known from DFT calculations.[48] This is somewhat opposite of the general perception of weaker oxygen binding in favor of higher catalytic activity for oxygen reduction reaction.[23,26] This situation also pertains to phase-segregated PdNi NPs where interatomic distances in Pd-rich nanophase are longer than those in Ni-rich nanophase rendering the former more catalytically active than the latter. Second, the average first CNs of site "A" atoms are relatively higher than those for site "B" atoms. The increased average first CNs of surface Pd atoms for Pd−Pd and Pd−Ni coordination would lead to a lower propensity of poisoning of the surface active sites.

4. CONCLUSIONS

In summary, PdNi nanoalloy catalysts have been shown to exhibit remarkable tunability in terms of phase state, bimetallic composition, and atomic-scale structure, which are responsible for the origin of the structural synergy for CO oxidation reaction over the nanoalloy catalysts. Both the structural tunability and synergy are achieved by thermochemical treatments under controlled reactive/nonreactive atmosphere, leading to the changes in phase state and atomic-scale structure, including the first-neighbor interatomic distances and the coordination numbers for atoms at the nanoparticle surface. Surface sites with more atomic neighbors and longer first-neighbor separations are more active catalytically than those with fewer atomic neighbors and shorter first-neighbor separations. This type of synergy has not been identified previously in terms of phase state, nanoalloy composition, and atomic-scale structure by traditional studies based on d-band theory for CO oxidation over alloy catalysts. The increased interatomic distances are believed to be associated with d band upshift and an increase in the binding energy of oxygen as predicted by DFT.[23,24] Our study demonstrates that optimization of the first coordination sphere radii and numbers for surface atoms through changes in alloy composition and thermochemical treatment may be an important pathway toward a better design of nanoalloy catalysts for a wide range of catalytic reactions. This endeavor can be helped with advanced techniques such as high-energy XRD coupled to atomic PDFs analysis for nanophase identification and atomic structure characterization.

■ ASSOCIATED CONTENT

Ⓢ Supporting Information

Additional experimental data. This material is available free of charge via the Internet at http://pubs.acs.org.

AUTHOR INFORMATION

Corresponding Author

cjzhong@binghamton.edu

Present Address

#Science & Technology Division, Corning Inc., New York 14831, United States.

Notes

The authors declare no competing financial interest.

ACKNOWLEDGMENTS

REFERENCES

(1) Zhang, H.; Jin, M. S.; Xia, Y. N. *Chem. Soc. Rev.* **2012**, *41*, 8035−8049.

(2) Zhang, H. J.; Watanabe, T.; Okumura, M.; Haruta, M.; Toshima, N. *Nat. Mater.* **2012**, *11*, 49−52.

(3) Hutchings, G. J. *Dalton Trans.* **2008**, 5523−5536.

(4) Chen, M. S.; Kumar, D.; Yi, C. W.; Goodman, D. W. *Science* **2005**, *310*, 291−293.

(5) Gao, F.; Goodman, D. W. *Chem. Soc. Rev.* **2012**, *41*, 8009−8020.

(6) Hutchings, G. J.; Kiely, C. J. *Acc. Chem. Res.* **2013**, *46*, 1759−1772.

(7) Shao, M. H.; Sasaki, K.; Adzic, R. R. *J. Am. Chem. Soc.* **2006**, *128*, 3526−3527.

(8) Shao, M.; Shoemaker, K.; Peles, A.; Kaneko, K.; Protsailo, L. *J. Am. Chem. Soc.* **2010**, *132*, 9253−9255.

(9) Enache, D. I.; Edwards, J. K.; Landon, P.; Solsona-Espriu, B.; Carley, A. F.; Herzing, A. A.; Watanabe, M.; Kiely, C. J.; Knight, D. W.; Hutchings, G. J. *Science* **2006**, *311*, 362−365.

(10) Kesavan, L.; Tiruvalam, R.; Ab Rahim, M. H.; bin Saiman, M. I.; Enache, D. I.; Jenkins, R. L.; Dimitratos, N.; Lopez-Sanchez, J. A.; Taylor, S. H.; Knight, D. W.; Kiely, C. J.; Hutchings, G. J. *Science* **2011**, *331*, 195−199.

(11) Antolini, E. *J. Power Sources* **2007**, *170*, 1−12.

(12) Cargnello, M.; Jaen, J. J. D.; Garrido, J. C. H.; Bakhmutsky, K.; Montini, T.; Gamez, J. J. C.; Gorte, R. J.; Fornasiero, P. *Science* **2012**, *337*, 713−717.

(13) Paalanen, P.; Weckhuysen, B. M.; Sankar, M. *Catal. Sci. Technol.* **2013**, *3*, 2869−2880.

(14) Ward, T.; Delannoy, L.; Hahn, R.; Kendell, S.; Pursell, C. J.; Louis, C.; Chandler, B. D. *ACS Catal.* **2013**, *3*, 2644−2653.

(15) Greeley, J.; Stephens, I. E. L.; Bondarenko, A. S.; Johansson, T. P.; Hansen, H. A.; Jaramillo, T. F.; Rossmeisl, J.; Chorkendorff, I.; Nørskov, J. K. *Nat. Chem.* **2009**, *1*, 552−556.

(16) Jin, C. C.; Sun, X. J.; Chen, Z. D.; Dong, R. L. *Mater. Chem. Phys.* **2012**, *135*, 433−437.

(17) Shen, S. Y.; Zhao, T. S.; Xu, J. B.; Li, Y. S. *J. Power Sources.* **2010**, *195*, 1001−1006.

(18) Persson, K.; Ersson, A.; Jansson, K.; Iverlund, N.; Jaras, S. *J. Catal.* **2005**, *231*, 139−150.

(19) Khanra, B. C.; Bertolini, J. C.; Rousset, J. L. *J. Mol. Catal. A: Chem.* **1998**, *129*, 233−240.

(20) Yang, L. F.; Shan, S.; Loukrakpam, R.; Petkov, V.; Ren, Y.; Wanjala, B. N.; Engelhard, M. H.; Luo, J.; Yin, J.; Chen, Y. S.; Zhong, C. J. *J. Am. Chem. Soc.* **2012**, *134*, 15048−15060.

(21) Shan, S.; Petkov, V.; Yang, L. F.; Mott, D.; Wanjala, B. N.; Cai, F.; Chen, B. H.; Luo, J.; Zhong, C. J. *ACS Catal.* **2013**, *3*, 3075−3085.

(22) Xu, W. J.; Cheng, D. J.; Niu, M.; Shao, X. H.; Wang, W. C. *Electrochim. Acta* **2012**, *76*, 440−445.

(23) Lim, F. C. H.; Zhang, J.; Jin, H. M.; Sullivan, M. B.; Wu, P. *Appl. Catal., A* **2013**, *451*, 79−85.

(24) Tang, W. J.; Zhang, L.; Henkelman, G. *J. Phys. Chem. Lett.* **2011**, *2*, 1328−1331.

(25) Liu, X.; Meng, C. G.; Han, Y. *J. Phys. Chem. C* **2013**, *117*, 1350−1357.

(26) Filhol, J. S.; Simon, D.; Sautet, P. *Surf. Sci.* **2001**, *472*, L139−L144.

(27) Chen, Y. G.; Zhuang, L.; Lu, J. T. *Chin. Chem. Lett.* **2007**, *18*, 1301−1304.

(28) Engel, T.; Ertl, G. *J. Chem. Phys.* **1978**, *69*, 1267−1281.

(29) Wang, F. G.; Zhang, H. J.; He, D. N. *Environ. Technol.* **2014**, *35*, 347−354.

(30) Hungria, A. B.; Calvino, J. J.; Anderson, J. A.; Martinez-Arias, A. *Appl. Catal., B* **2006**, *62*, 359−368.

(31) Petkov, V.; Shan, S.; Chupas, P.; Yin, J.; Yang, L. F.; Luo, J.; Zhong, C. J. *Nanoscale* **2013**, *5*, 7379−7387.

(32) Petkov, V.; Wanjala, B. N.; Loukrakpam, R.; Luo, J.; Yang, L. F.; Zhong, C. J.; Shastri, S. *Nano Lett.* **2012**, *12*, 4289−4299.

(33) Petkov, V.; Yang, L.; Yin, J.; Loukrakpam, R.; Shan, S.; Wanjala, B.; Luo, J.; Chapman, K. W.; Zhong, C. J. *Phys. Rev. Lett.* **2012**, *109*, 125504.

(34) Petkov, V.; Shastri, S.; Shan, S.; Joseph, P.; Luo, J.; Zhong, C. J.; Nakamura, T.; Herbani, Y.; Sato, S. *J. Phys. Chem. C* **2013**, *117*, 22131−22141.

(35) Yin, J.; Shan, S.; Ng, M. S.; Yang, L. F.; Mott, D.; Fang, W.; Kang, N.; Luo, J.; Zhong, C. J. *Langmuir* **2013**, *29*, 9249−9258.

(36) Luo, J.; Kariuki, N.; Han, L.; Wang, L.; Zhong, C. J.; He, T. *Electrochim. Acta* **2006**, *51*, 4821−4827.

(37) Oxford, S. M.; Lee, P. L.; Chupas, P. J.; Chapman, K. W.; Kung, M. C.; Kung, H. H. *J. Phys. Chem. C* **2010**, *114*, 17085−17091.

(38) Egami, T.; Billinge, S.J. L. *Underneath the Braggs' Peak*; Pergamon: Amsterdam, The Netherlands, 2003.

(39) Petkov, V. *Mater. Today* **2008**, *11*, 28−38.

(40) Iglesias-Juez, A.; Hungria, A. B.; Martinez-Arias, A.; Anderson, J. A.; Fernandez-Garcia, M. *Catal. Today* **2009**, *143*, 195−202.

(41) Gaudet, J. R.; de la Riva, A.; Peterson, E. J.; Bolin, T.; Datye, A. K. *ACS Catal.* **2013**, *3*, 846−855.

(42) Berlowitz, P. J.; Peden, C. H. F.; Goodman, D. W. *J. Phys. Chem.* **1988**, *92*, 5213−5221.

(43) Loukrakpam, R.; Luo, J.; He, T.; Chen, Y.; Xu, Z.; Njoki, P. N.; Wanjala, B. N.; Fang, B.; Mott, D.; Yin, J.; Klar, J.; Powell, B.; Zhong, C. J. *J. Phys. Chem. C* **2011**, *115*, 1682−1694.

(44) Wanjala, B. N.; Fang, B.; Luo, J.; Chen, Y. S.; Yin, J.; Engehard, M. H.; Loukrakpam, R.; Zhong, C. J. *J. Am. Chem. Soc.* **2011**, *133*, 12714−12727.

(45) Wanjala, B. N.; Fang, B.; Loukrakpam, R.; Chen, Y. S.; Engelhard, M.; Luo, J.; Yin, J.; Yang, L. F.; Shan, S.; Zhong, C. J. *ACS Catal.* **2012**, *2*, 795−806.

(46) Wanjala, B. N.; Fang, B.; Shan, S. Y.; Petkov, V.; Zhu, P. Y.; Loukrakpam, R.; Chen, Y. S.; Luo, J.; Yin, J.; Yang, L. F.; Shao, M. H.; Zhong, C. J. *Chem. Mater.* **2012**, *24*, 4283−4293.

(47) Loukrakpam, R.; Shan, S. Y.; Petkov, V.; Yang, L. F.; Luo, J.; Zhong, C. J. *J. Phys. Chem. C* **2013**, *117*, 20715−20721.

(48) Miller, J. T.; Kropf, A. J.; Zha, Y.; Regalbuto, J. R.; Delannoy, L.; Louis, C.; Bus, E.; van Bokhoven, J. A. *J. Catal.* **2006**, *240*, 222−234.

7151

dx.doi.org/10.1021/ja5026744 | *J. Am. Chem. Soc.* 2014, 136, 7140−7151